Appl Compos Mater (2016) 23:271–288
DOI 10.1007/s10443-015-9460-5

A Static Burst Test for Composite Flywheel Rotors

Stefan Hartl[1] · Alexander Schulz[1] · Harald Sima[1] · Thomas Koch[2] · Manfred Kaltenbacher[1]

Received: 13 July 2015 / Accepted: 21 July 2015 / Published online: 18 August 2015

Abstract High efficient and safe flywheels are an interesting technology for decentralized energy storage. To ensure all safety aspects, a static test method for a controlled initiation of a burst event for composite flywheel rotors is presented with nearly the same stress distribution as in the dynamic case, rotating with maximum speed. In addition to failure prediction using different maximum stress criteria and a safety factor, a set of tensile and compressive tests is carried out to identify the parameters of the used carbon fiber reinforced plastics (CFRP) material. The static finite element (FE) simulation results of the flywheel static burst test (FSBT) compare well to the quasistatic FE-simulation results of the flywheel rotor using inertia loads. Furthermore, it is demonstrated that the presented method is a very good controllable and observable possibility to test a high speed flywheel energy storage system (FESS) rotor in a static way. Thereby, a much more expensive and dangerous dynamic spin up test with possible uncertainties can be substituted.

Keywords Flywheel energy storage systems · Polymer-matrix composites · Finite element analysis · Filament winding

1 Introduction

Flywheel energy storage systems (FESS) represent an ecologically and economically sustainable technology for decentralized energy storage. Long life cycles without performance

✉ Stefan Hartl
stefan.hartl@tuwien.ac.at

[1] Institute of Mechanics and Mechatronics, Vienna University of Technology, Getreidemarkt 9 (BA06), 1060 Wien, Austria

[2] Institute of Materials Science and Technology, Vienna University of Technology, Getreidemarkt 9 (BE03), 1060 Wien, Austria

degradation depending on depth of discharge (DoD) and a minimum of systematic maintenance are key advantages of this technology. Thereby, we have developed a new flywheel rotor geometry utilizing very high energy density along with the required manufacturing technology. To achieve high energy densities, the rotor of FESS are usually manufactured of fiber reinforced plastics (FRP) by the filament winding process. Especially carbon fiber reinforced plastics (CFRP) show a high specific strength ratio, which enable tip speeds up to 1000 m/s. These high rotational speeds cause high kinetic energy and so fragments of the rotor can do serious damage to structures and people in case of a burst event. To compensate for possible unknowns, e.g. the real fiber volume fraction or manufacturing imperfections due to the filament winding process a safety factor for calculation is usually used. The goal is to reduce this safety factor and use the full capability of the material to maximize the energy density as well as the energy efficiency of the FESS.

Hence, a burst test under controlled conditions is necessary to ensure a safe operation. A standard procedure to test the composite part of a rotor is a dynamic spin up under operating conditions till a burst event occurs. On one hand this causes immense costs for testing and on the other hand it is critical with regards to safety. Therefore, other methods for the burst test have been developed. In [1, 2], the composite rotor is mounted in a proper spin test system. The one-sided bearing can be disadvantageous in case of large rotors because of the changed rotordynamic behaviour and possible unbalance forces during spin up. A similar setup is used to test disk and cylinder like composite rotors [3–5]. In [6, 7] a test method for the evaluation of CFRP materials is described. In both setups an elastic-plastic hub is used to drive the CFRP rotor to the burst event. A main disadvantage of a dynamic spin test is the reduced controllability and observability of the burst event compared to a static burst test. The major challenge of static testing is the application of loads sufficiently similar to inertia loads arising due to the rotation which is typically not possible. A test to burst hoop filament wounded rings is presented in [8–10]. Similar tests to burst hoop wounded and angle ply tubes are shown in [11–14]. These hydroburst test methods use pressure applied by temperature rise or explosive charge on the inside to expand and thereby burst the rings or tubes.

The special patented geometry [15, 16] of the CFRP hoop wound rotor is shown in Fig. 1. The shape of the CFRP rotor is a result of a two-step energy density optimization. In the first step a genetic algorithm is used to find the optimum shape of the flywheel rotor. Based on these results characteristic parameters are derived and a combined strength safety factor and rotordynamic optimization is carried out in the second step. The stress state of this FESS rotor is a linear combination of the thermal press-fitting process and the inertial load due to rotation. With a safety margin of two, an energy density of 29 Wh/kg at a rotor speed of 17000 rpm can be reached with this setup, compared to 16 Wh/kg for a conventional H-shaped rotor geometry or 18 Wh/kg for a press-fitted multi-ring assembly [17] with rectangular cross-section in combination with a CFRP hollow shaft [18]. The challenges of a flywheel static burst test (FSBT) are to achieve at an identical failure point, quantitatively identical stress state and deformation equivalence compared to the dynamic burst test.

Within the presented paper a FSBT method for composite FESS rotors is presented. This method is a safe alternative to a dynamic spin test, and because of the quasistatic loading the burst event is better observable. Another advantage is the better possibility to analyze the burst fragments, e.g. by a scanning electron microscope (SEM). Thereby, many different approaches have been analyzed through static finite element (FE) simulation compared with

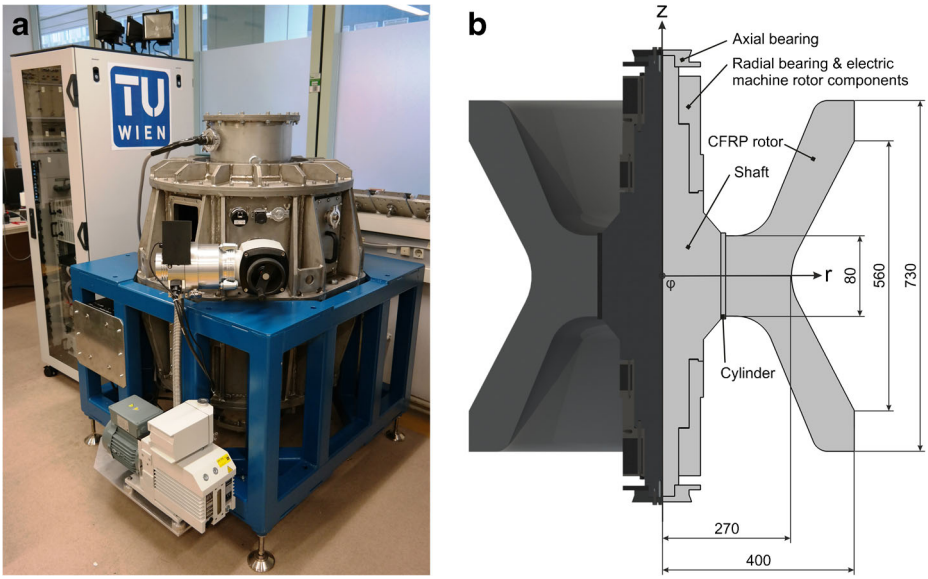

Fig. 1 7 kWh FESS: **a** Flywheel test rig [19]; **b** Geometry of a 7 kWh flywheel rotor consisting of the CFRP rotor mass, shaft (aluminium), bearing and motor components (soft magnetic iron) and a steel cylinder to optimize the press-fitting process; dimensions in mm

a previously optimized flywheel geometry as a starting point for dynamic FE-simulation at full speed of the rotor. Furthermore, the material parameter of the used CFRP have been identified to perform correct FE-simulations.

The rest of the paper is organized as follows. In Section 2.1 we present our new approach for the static burst test. The material parameter identification is shown in Section 2.2. The composite modeling and the FE-models are explained in Section 2.3. In Section 2.4 the simulation results are shown. In Section 2.5 the experimental setup is described, followed by a detailed discussion of the achieved results in Section 3. The paper closes with a conclusion.

2 Materials and Methods

2.1 A New Static Burst Test Approach

The developed flywheel static burst test (FSBT) uses the CFRP rotor of the optimized 7 kWh FESS rotor, as shown in Fig. 1b to test exactly the same geometry in a static way. Therefore specially designed load transfer elements that are optimized for maximum stiffness in pulling direction are used. This optimization was carried out by using the solid isotropic material with penalisation (SIMP) method. On one rotor side a cutout has been made for force application by the load transfer elements. The equivalent cutted CFRP rotor and the two load transfer elements are shown in Fig. 2.

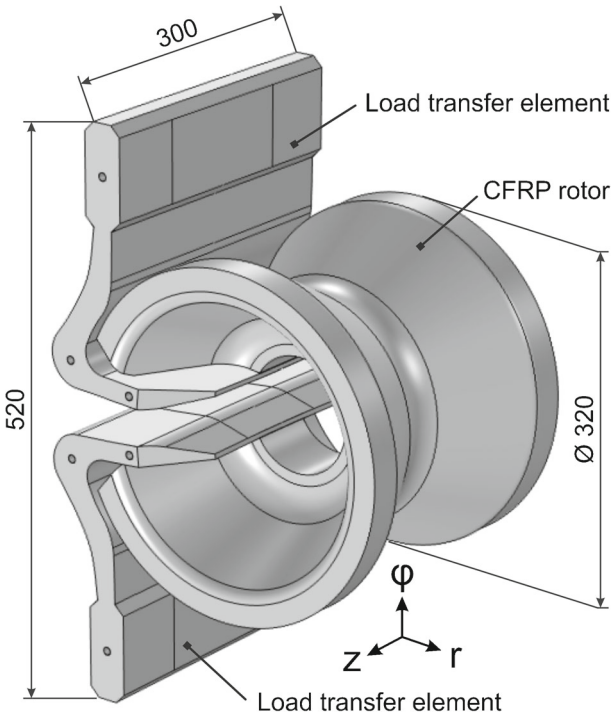

Fig. 2 FSBT geometry consisting of the load transfer elements (steel) and the CFRP rotor; dimensions in mm

To reduce the required pulling force, e.g. provided by a tensile test machine, an isotropic geometry scaling factor of $\chi = 0.4$ for the CFRP rotor is used. Therefore, a 250 kN universal tensile test machine can be used to burst the CFRP rotor. A difference to the dynamic case is the absence of the whole shaft and steel components. This can influence the results, but as prestressing due to thermal press-fitting increases ultimate strength [20], the FSBT is a more conservative test method. For calculation of the stress state and deformations the finite element software COMSOL was used. The postprocessing such as determination of the failure criteria, was done using MATLAB.

2.2 Material Parameter Identification

At the beginning, a broad range of different fiber/matrix combinations has been tested in a nondestructive way [21] to determine the in-plane stiffness behavior of the used unidirectional CFRP. Out of these results the combination T800H/LY1564/3487 was selected as rotor material due to the low stiffness transverse to the fiber direction, that leads to a reduced stress distribution in radial direction of the rotor during operation. To get the CFRP material data, tensile test specimen were produced using the same manufacturing process as for the flywheel rotor applying wet winding technique with the material and process parameters given in Table 1. The material parameters were measured by a set of tensile-/compressive tests on flatcoupon [22–25], cylindric and ring specimen, see Fig. 3. The measured parameters are summarized in Table 2.

Table 1 Material and process parameters of fiber and resin

TORAY Torayca T800H	HUNTSMAN Araldite LY1564/Aradur 3487	
	Fiber	Resin
Tensile strength, MPa	5490	76
Tensile modulus, GPa	294	3.1
Elongation at break, %	1.9	4.9
Density, kg/m^3	1810	1100
Filament diameter, μm	5	–
Tow size	12K	–
Tex	445	–
Curing schedule	1st: 2h/80 °C, 2nd: 6h/120 °C, 3rd: 1h/60 °C	

2.3 Modeling

2.3.1 Composite Modeling

In the following simulations a hoop wound structure using a filament winding process with a fiber angle of 90° between the fibers and the axis of rotation is assumed. Hence, the stiffness tensor $\boldsymbol{E}$ and its entries, given in Eqs. 1, 2 and 3, can be expressed by use of five independent constants, given and described in Table 2.

$$\boldsymbol{E} = \begin{bmatrix} E_{\varphi\varphi} & E_{\varphi r} & E_{\varphi z} & 0 & 0 & 0 \\ & E_{rr} & E_{rz} & 0 & 0 & 0 \\ & & E_{zz} & 0 & 0 & 0 \\ & & & G_{\varphi r} & 0 & 0 \\ & sym. & & & G_{\varphi r} & 0 \\ & & & & & G_{rz} \end{bmatrix} \tag{1}$$

$$\Delta = \frac{1 - 2\nu_{\varphi r}\nu_{r\varphi} - 2\nu_{r\varphi}\nu_{rz}\nu_{\varphi r} - \nu_{rz}^2}{E_\varphi E_r^2} \tag{2}$$

$$\begin{aligned} G_{rz} &= \tfrac{E_r}{2(1+\nu_{rz})}, & \tfrac{\nu_{ij}}{E_i} &= \tfrac{\nu_{ji}}{E_j}, \quad i,j = \varphi, r, z, \\ E_{\varphi\varphi} &= \tfrac{1-\nu_{rz}^2}{E_r^2\Delta}, & E_{\varphi r} &= \tfrac{\nu_{r\varphi}+\nu_{r\varphi}\nu_{rz}}{E_r^2\Delta}, \\ E_{rr} &= \tfrac{1-\nu_{\varphi r}\nu_{r\varphi}}{E_\varphi E_r\Delta}, & E_{rz} &= \tfrac{\nu_{rz}+\nu_{\varphi r}\nu_{r\varphi}}{E_\varphi E_r\Delta}, \\ E_{zz} &= \tfrac{1-\nu_{\varphi r}\nu_{r\varphi}}{E_\varphi E_r\Delta}, & E_{\varphi z} &= \tfrac{\nu_{r\varphi}+\nu_{r\varphi}\nu_{rz}}{E_r^2\Delta}. \end{aligned} \tag{3}$$

2.3.2 Failure Criteria for Composite Laminates and Safety Factor

To investigate the failure of the presented models, several failure criteria have been used. For simple evaluating of material failure the maximum stress criteria expressed in Eq. 4 can be applied. Once the normal stress in principal material directions (radial, hoop, rz-plane) reach their corresponding maximum strengths (Y_t, X_t, S_{23}), material failure can be expected.

$$\frac{\sigma_r}{Y_t} \geq 1, \quad \frac{\sigma_\varphi}{X_t} \geq 1, \quad \frac{\sigma_{rz}}{S_{23}} \geq 1\,. \tag{4}$$

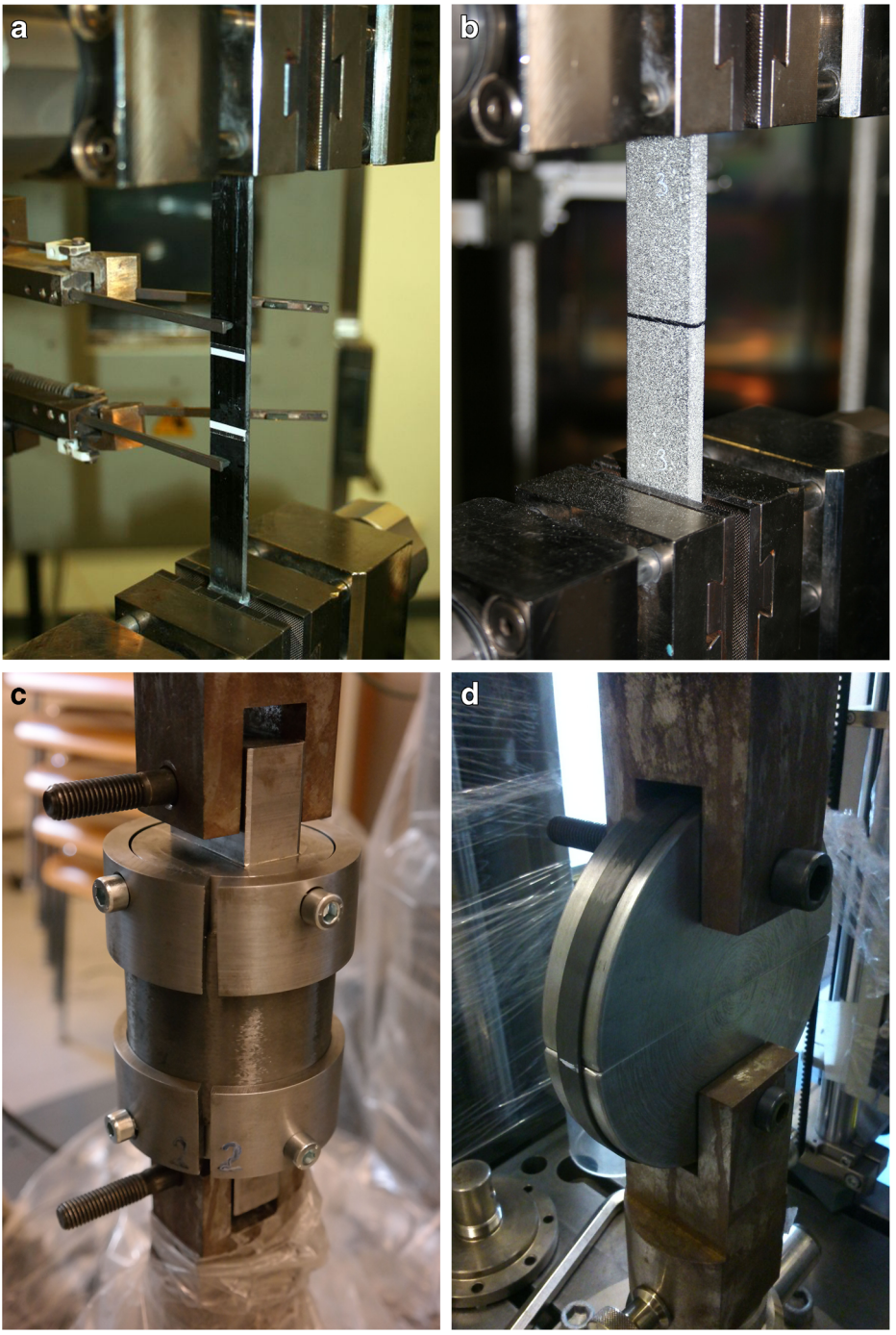

Fig. 3 Testing T800H/LY1564/3487: **a** Tensile-/compressive test in fiber direction; **b** Tensile-/compressive test transverse to fiber direction; **c** Tensile test in axial direction on cylindric specimen; **d** Tensile test in hoop direction on ring specimen

Table 2 Measured material data for T800H/LY1564/3487 specimens with a fiber volume fraction of 60 % and metal material data used for simulation

T800H/LY1564/3487		
Elastic modulus radial r, GPa	E_r	7.8
Elastic modulus hoop φ, GPa	E_φ	139
Elastic modulus axial z, GPa	E_z	7.8
Poissons ratio	$\nu_{\varphi r}$	0.41
Poissons ratio	ν_{zr}	0.38
Shear modulus φr, GPa	$G_{\varphi r}$	3.4
Tensile strength φ, MPa	X_t	1815
Compressive strength φ, MPa	X_c	650
Tensile strength r, z, MPa	Y_t, Z_t	24
Compressive strength r, z, MPa	Y_c, Z_c	113
Shear strength φr, MPa	S_{12}	57
Shear strength φz, MPa	S_{13}	57
Shear strength rz, MPa	S_{23}	14
Steel		
Elastic modulus, GPa	E_{St}	210
Poissons ratio	ν_{St}	0.3
Von mises strength, MPa	$\sigma_{V,St}$	690
Aluminium		
Elastic modulus, GPa	E_{Al}	70
Poissons ratio	ν_{Al}	0.3
Von mises strength, MPa	$\sigma_{V,Al}$	500

This criterion does not consider interactions between the stress components of the given stress state. For a more reliable failure estimation with consideration of the inter-stress effect, the generalized quadratic Tsai-Wu criterion [26] was considered, which reads as

$$\overline{\boldsymbol{F}}^T \boldsymbol{\sigma} + \boldsymbol{\sigma}^T \widetilde{\boldsymbol{F}} \boldsymbol{\sigma} \geq 1 \,. \tag{5}$$

The stress state vector $\boldsymbol{\sigma}$ and $\overline{\boldsymbol{F}}$, $\widetilde{\boldsymbol{F}}$ the second and fourth order tensor of the strength parameters out of Table 2 are given as follows

$$\boldsymbol{\sigma} = \begin{bmatrix} \sigma_\varphi \\ \sigma_r \\ \sigma_z \\ \sigma_{rz} \\ \sigma_{\varphi r} \\ \sigma_{\varphi z} \end{bmatrix}, \quad \overline{\boldsymbol{F}} = \begin{bmatrix} F_1 \\ F_2 \\ F_3 \\ 0 \\ 0 \\ 0 \end{bmatrix}, \tag{6}$$

$$\widetilde{\boldsymbol{F}} = \begin{bmatrix} F_{11} & F_{12} & F_{13} & 0 & 0 & 0 \\ & F_{22} & F_{23} & 0 & 0 & 0 \\ & & F_{33} & 0 & 0 & 0 \\ & & & F_{44} & 0 & 0 \\ & & & & F_{55} & 0 \\ sym. & & & & & F_{66} \end{bmatrix}, \tag{7}$$

$$
\begin{aligned}
F_1 &= \tfrac{1}{X_t} - \tfrac{1}{X_c}, & F_2 &= \tfrac{1}{Y_t} - \tfrac{1}{Y_c},\\
F_3 &= \tfrac{1}{Z_t} - \tfrac{1}{Z_c}, & F_{11} &= \tfrac{1}{X_t X_c},\\
F_{22} &= \tfrac{1}{Y_t Y_c}, & F_{33} &= \tfrac{1}{Z_t Z_c},\\
F_{44} &= \tfrac{1}{S_{23}^2}, & F_{55} &= \tfrac{1}{S_{13}^2},\\
F_{66} &= \tfrac{1}{S_{12}^2}, & F_{12} &= -\tfrac{1}{2}\sqrt{F_{11}F_{22}},\\
F_{13} &= -\tfrac{1}{2}\sqrt{F_{11}F_{33}}, & F_{23} &= -\tfrac{1}{2}\sqrt{F_{33}F_{22}}.
\end{aligned}
\tag{8}
$$

The safety factor S is introduced as a proportional factor as follows

$$\boldsymbol{\sigma}^* = S\boldsymbol{\sigma}\,. \tag{9}$$

Thereby, S links the actual stress state $\boldsymbol{\sigma}$ and the stress state $\boldsymbol{\sigma}^*$ that causes material failure. Combining (5) and (9) and defining $\boldsymbol{\sigma}^* = \boldsymbol{\sigma}$ results in a quadratic equation with the following (positive) solution for the safety factor

$$S = \frac{-\overline{\boldsymbol{F}}^T\boldsymbol{\sigma} + \sqrt{(\overline{\boldsymbol{F}}^T\boldsymbol{\sigma})^2 + 4\boldsymbol{\sigma}^T\widetilde{F}\boldsymbol{\sigma}}}{2\boldsymbol{\sigma}^T\widetilde{F}\boldsymbol{\sigma}}. \tag{10}$$

A safety factor of $S \leq 1$ indicates material failure. In this study the maximum stress criteria and the inverse safety factor are used to study the burst event and the failure mode.

2.3.3 FE-models

The axisymmetric geometry of the nonlinear dynamic model of the rotor is discretized by quadrilateral finite elements with bilinear basis functions and using the $r\varphi$- symmetry plane as roller boundary condition, see Fig. 4a. The CFRP rotor is assumed to be transversely isotropic in hoop direction. In Table 2 the used material parameters for the CFRP rotor and the shaft components are summarized. The stress state of this FESS was calculated in two steps. In the first step the thermal shrink fit of the shaft onto the rotor and in the second step the inertial loads due to rotation was computed.

For static FE-simulation of the FSBT, a 3-dimensional model of the isotropic scaled ($\chi = 0.4$) CFRP rotor (see Fig. 1b) using two symmetry planes as roller boundary condition to reduce simulation effort has been used. The model is discretized by quadratic tetragonal finite elements (see Fig. 4c) and the CFRP rotor is assumed to be transversely isotropic in hoop direction. The material parameters for the scaled CFRP rotor and load transfer elements made of steel are given in Table 2. Modeling of the contact between the load transfer elements and the rotor was neglected, as the observed failure point is far away from the contact area and therefore has minimal influence and so a linear simulation has been performed.

For both models a mesh convergence study has been performed to check for the influence of mesh type and size onto the Tsai-Wu criterion in the predicted failure point.

2.4 Simulation Results

2.4.1 Stress Distribution in the 7 kWh FESS Rotor

The dynamic simulation results of the 7 kWh FESS rotor without considering the shaft region are shown in Fig. 4a. The minimum safety factor ($S = 1$) appears on the inner

radius between the shaft interface and the cantilever part of the CFRP rotor at a radial position of $r = 69$ mm. The analysis of the maximum stress criterion along the dashed line illustrates that the radial stress σ_r is the critical factor. A failure occurs when the rotor speed is increased over the value which leads to a safety factor of $S = 1$. This happens at a rotor

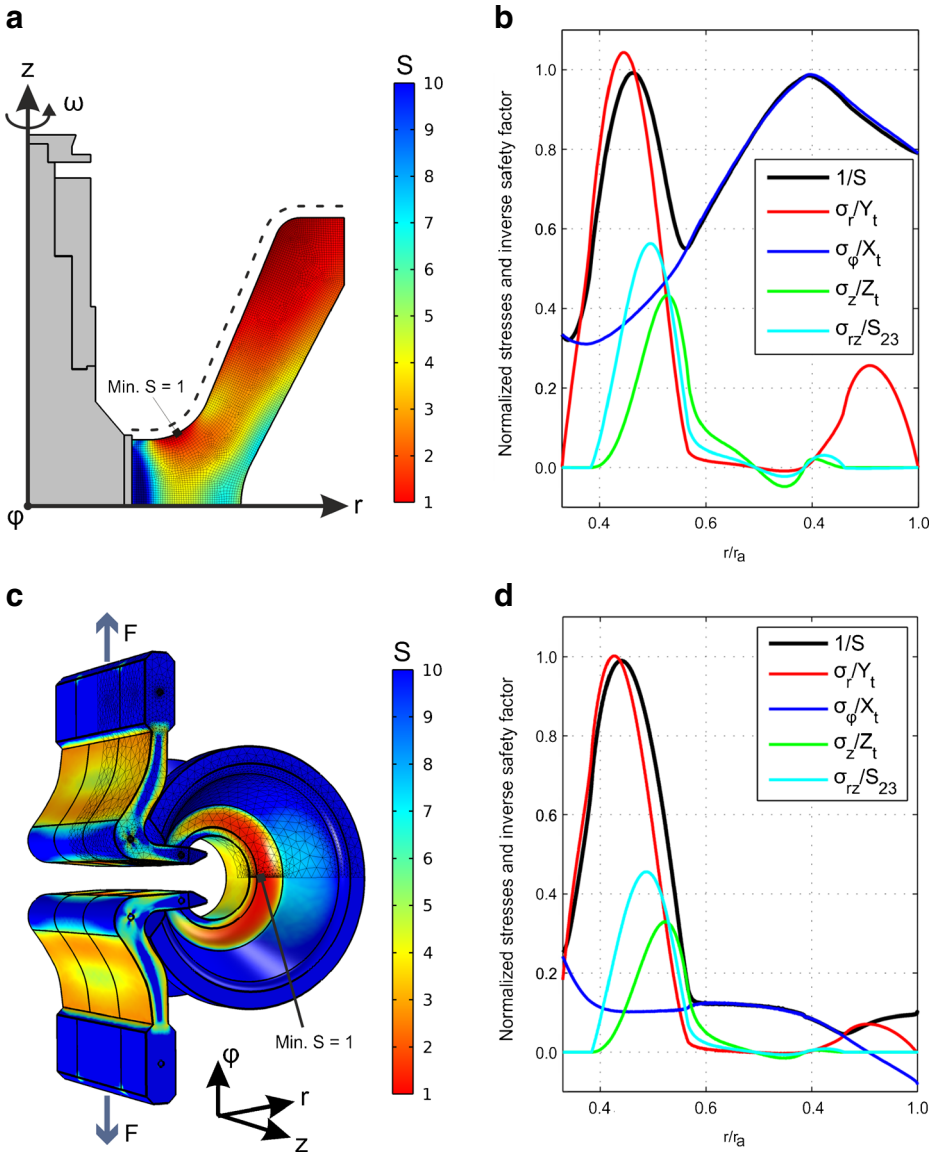

Fig. 4 Simulation results: **a** 7 kWh FESS rotor, safety factor S evaluated at $\omega = 2590\,\mathrm{s}^{-1}$; **b** 7 kWh FESS rotor, normalized stresses and inverse safety factor evaluated at $\omega = 2590\,\mathrm{s}^{-1}$ on the upper boundary of the CFRP rotor, $r_a = 400$ mm; **c** FSBT, safety factor S evaluated at $F = 43$ kN; **d** FSBT, normalized stresses and inverse safety factor evaluated for $F = 43$kN on the upper boundary of the CFRP rotor, $r_a = 160$ mm. Safety factors calculated based on Eq. 10

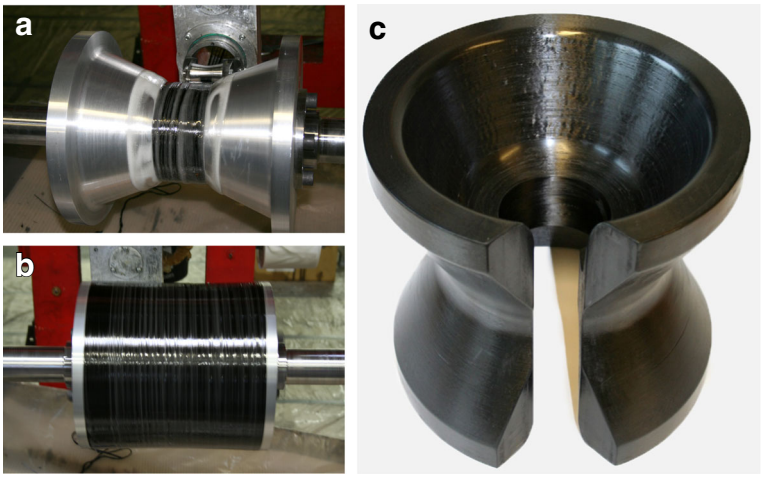

Fig. 5 Fabrication of the test specimen: **a** aluminum mandrel; **b** finished winding operation; **c** turned and milled specimen

speed of $\omega = 2590\,\mathrm{s}^{-1}$, where the radial stress σ_r is equal to the maximum tensile strength Y_t, see Fig. 4b.

2.4.2 Stress Distribution in FSBT

The FSBT simulation results are depicted in Fig. 4c. The minimum safety factor $S = 1$ can be found on the inner radius of the contour located at the used symmetry plane. The radial position is $r = 67\,\mathrm{mm}$. If the load is increased above 43 kN, a failure occurs due to the radial stress σ_r that reaches the maximum tensile strength Y_t, see Fig. 4d.

2.4.3 Comparison of 7 kWh FESS Rotor and FSBT Results

The results of the static and dynamic simulation show very good agreement, as shown in Fig. 4b and 4d. The position, where the failure occurs, is nearly identical. The inverse safety factor shows one big difference at increasing radius. As one can see in Fig. 4b, the curve is rising but is still lower than at the predicted failure point. The analysis shows that the safety factor can mainly be approximated by the combination of the radial- and hoop maximum stress criteria.

2.5 Experimental Setup

2.5.1 Specimen Fabrication

The hoop wound specimen of the flywheel rotor was produced using the same wet winding technique with the same process parameters as for material identification, given in Table 1. Winding was done using an aluminum mandrel that has been machined to get the inner rotor contour. The specimen together with the mandrel were then placed into a temperature-controlled oven for curing. After curing and before removing the specimen from the mandrel

the outer contour has been machined. Afterwards, the specimen was cut through on one side to serve space for the load transfer elements, see Fig. 5. The load transfer elements were cutted out of steel plates using a waterjet and then welded together to achieve the required width of 300 mm.

2.5.2 Test Procedure

For tensile testing a Zwick Z250 Universal Testing System with a load capacity of 250 kN was used. The specimen was placed between the two well centered load transfer elements, see Fig. 6. During the tensile test, the test speed of the testing machine was kept constant at a level of 1 mm/min and the load and strain data were measured until failure of the specimen.

2.5.3 Strain Measurement

The strains in radial-, hoop- and axial direction where measured by strain gauges on one side of the specimen direct at the location of the predicted failure point and optically by digital image correlation using a region of about 50 mm × 30 mm centered around the failure point

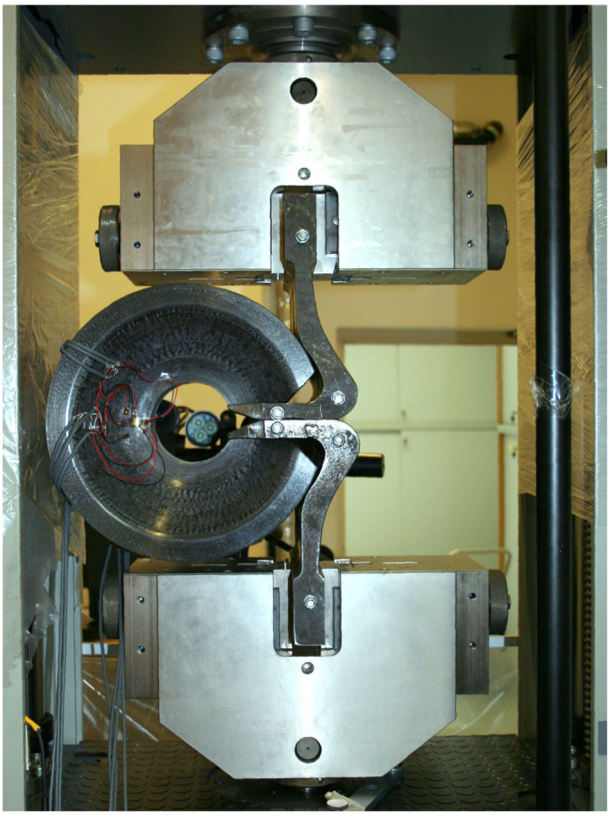

Fig. 6 Test machine setup; Zwick Z250 Universal Testing System, load transfer elements and the scaled CFRP rotor

on the other side of the specimen. Electrical and optical measurements were synchronized by measuring the crosshead travel of the testing machine.

Strain Gauge Measurement The used Hottinger Baldwin Messtechnik (HBM) strain gauge was directly applied at the predicted failure point, see Fig. 7. To measure the correct strain in radial- and hoop direction a strain gauge (rectangular rosette) with three measurement grids in 0°/45°/90° alignment, each in quarter bridge operation mode, was used. By combination of the three results the main strain direction and magnitude were calculated. The axial strain could not be measured at the failure point. Instead, the strain gauge was applied to the closest point on the innerst radius, as the simulation showed no difference between the analysis results of those two points. For data acquisition a HBM Spider8 amplifier and the HBM Catman® 3.0 software were used.

Optical Strain Measurement Digital image correlation (DIC) was used to perform a non-contact deformation measurement. The DIC software used in this experimental work was the ARAMIS DIC system, developed by Gesellschaft für optische Messtechnik (GOM), see Fig. 8. By use of a synchronized stereo camera system and a white colored stochastic

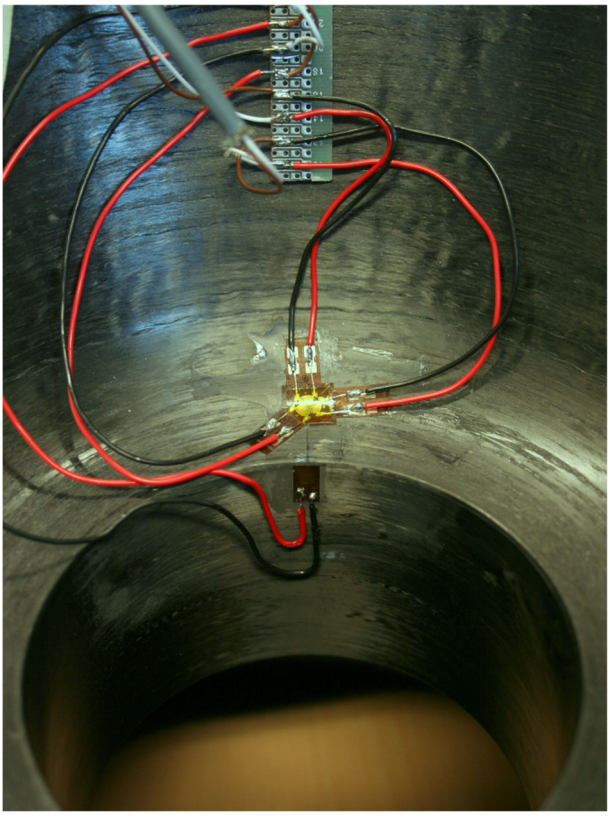

Fig. 7 Three channel strain gauge at the predicted failure point to measure radial- and hoop strain, strain gauge on the inner radius to measure the axial strain

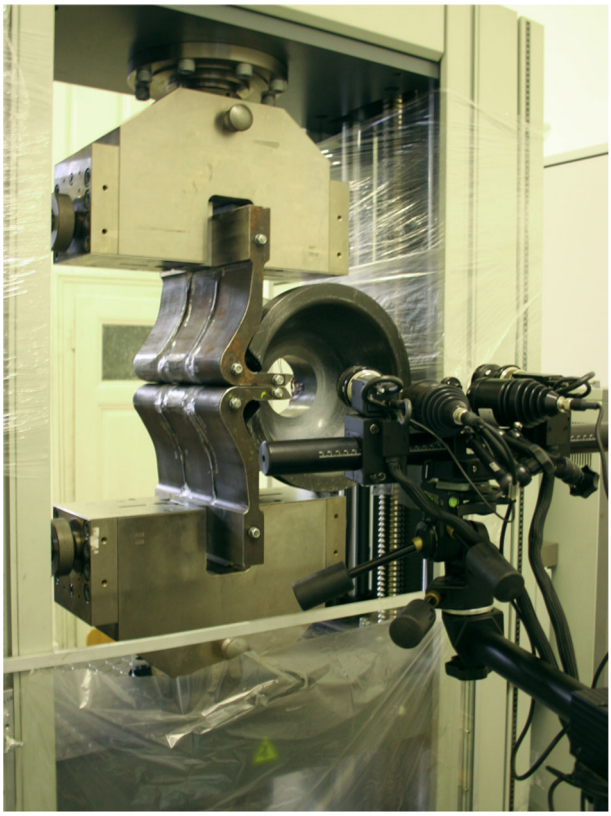

Fig. 8 GOM ARAMIS measurement setup, synchronized stereo cameras facing one specimen failure surface

pattern painted on the specimen it was possible to measure the deformation field in three dimensions after calibration.

3 Results and Discussion

3.1 Maximum Load and Strain Measurement

The result of the load measurement is depicted in Fig. 9. As can be seen, the curve is nonlinear with respect to the crosshead travel of the machine at the first 20 %. The system gets linear at an applied load of 10 kN. The maximum load until failure occurs is about 45 kN. Figure 9 shows the measured signals of the strain gauges. The radial strain reaches a maximum of 1.61 %. The hoop and axial strain reaches a magnitude of 0.13 % and −0.37 %, respectively. Then the radial failure occurs and splits the strain gauge, which is an indicator for a good failure point prediction. The optical strain measurement result for the expected failure point on the other specimen side can be seen in Fig. 10.

The absolute difference between the two measurement methods for hoop strains is about 0.2 % and 0.07 %. The optical measurement results of the observed area are depicted in

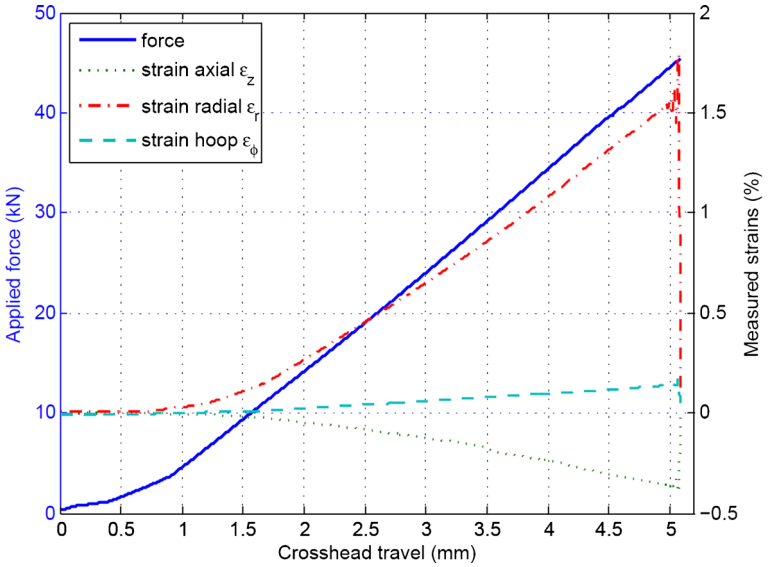

Fig. 9 Strain gauge measurement: strains in axial-, radial- and hoop direction and applied force as a function of the crosshead travel of the testing machine

Fig. 11. The images shown were taken directly before and directly after the critical load has been reached. This enables a perfect visualization of the crack that splits the rotor into two pieces. As can be seen, the crack occurs in the predicted area because of radial failure of the specimen.

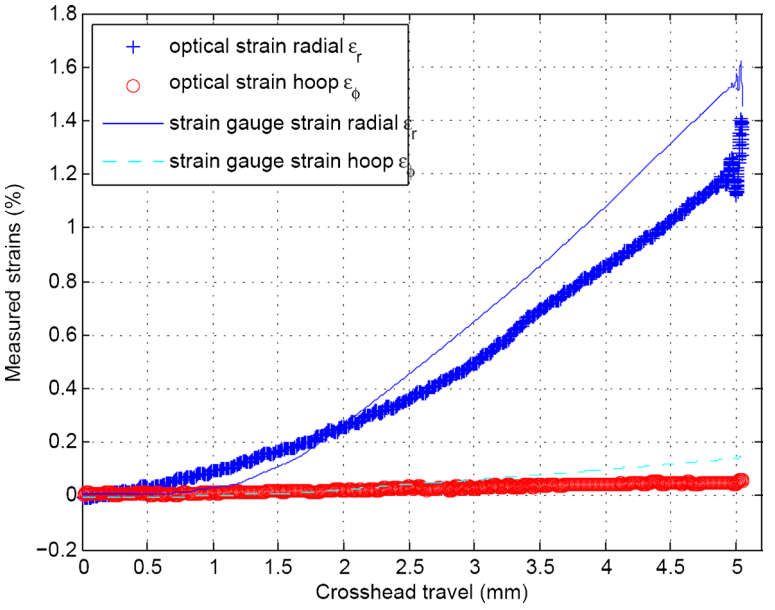

Fig. 10 Optically and strain gauge measured strains in radial and hoop direction as a function of the crosshead travel of the testing machine

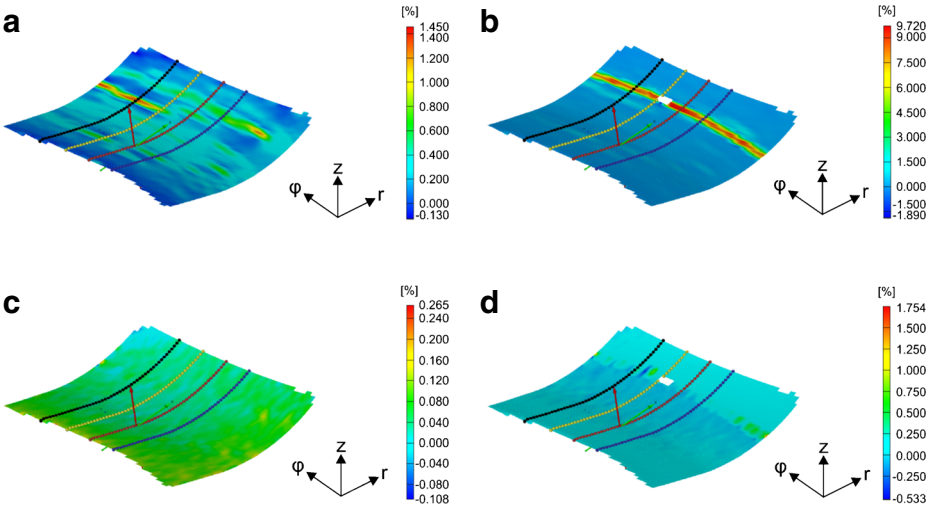

Fig. 11 Optical strain measurement results: **a** radial direction, one time step before burst occurs; **b** radial direction, after failure at $F = 45\,\text{kN}$; **c** hoop direction, one time step before burst occurs; **d** hoop direction, after failure at $F = 45\,\text{kN}$

3.2 Observation of the Failure Surface

Due to the fact that the carbon fiber/matrix interaction has a strong effect on strength, scanning electron microscope (SEM) observations of the interphase regions of the described CFRP system after the burst test were done, see Fig. 12. Thereby, a slice of 10 mm thickness was cut out of the failure region of the specimen. In some areas the resin fiber bond is rather weak, resulting in interface cracks. For these structures possible uncertainties like residual stresses [27] or imperfections on the surface [28] due to the manufacturing process

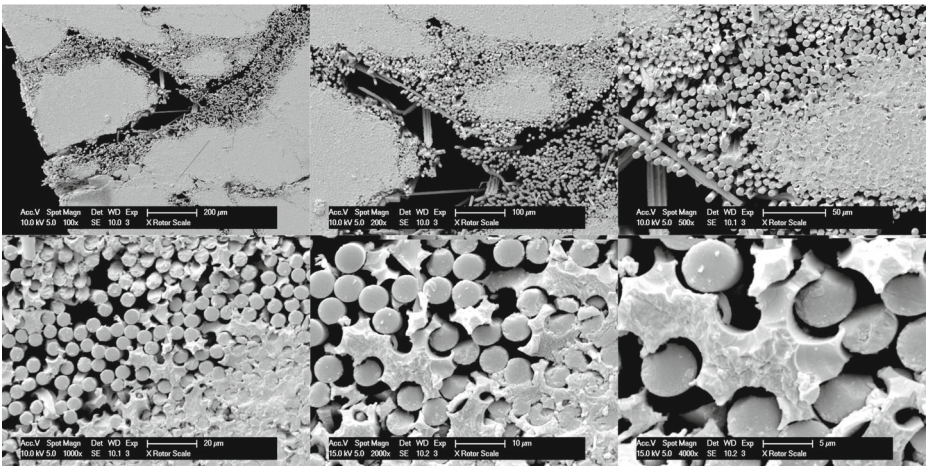

Fig. 12 Scanning electron microscope (SEM) results of the failure surface (magnification range: 100× to 4000×)

can be the reason. This causes a major decrease in radial direction strength and should be considered when choosing the fiber/matrix combination. The difference between weak and strong interfacial behavior was studied in [29–31].

3.3 FSBT compared to Simulation Results

The presented simulation result for the FSBT show a maximum load of $F = 43\,\text{kN}$ (see Section 2.4). The simulation was performed neglecting the contact between the load transfer elements and the scaled CFRP rotor. This does not affect the result in the failure point but the observed elastic deformation of the load transfer elements during the experiment showed a major difference compared to the simulation. The simulation showed no movement of the whole assembly transverse to the pulling direction that is caused by a stick-slip effect in the contact area and the low stiffness of the clamping unit compared to perfect boundary conditions in the simulation. In fact, the simulation result shows a lower maximum load of $F = 43\,\text{kN}$ that is in very good coincidence with the FSBT test procedure, where the rotor cracked at $F = 45\,\text{kN}$. Furthermore, the failure point of simulation and experimental result show very good agreement.

4 Conclusion

In this paper a flywheel static burst test (FSBT) to burst a carbon fiber reinforced plastic (CFRP) flywheel rotor with nearly the same stress distribution as in the dynamic case rotating with maximum speed is presented. Failure prediction was done using different maximum stress criteria and a safety factor calculated using the Tsai-Wu criterion. Dynamic simulation results of a 7 kWh FESS rotor and static simulation results of the FSBT are in very good agreement including the failure point as well as the stress distribution and the maximum load. To identify the parameters of the used CFRP-material, a set of tensile tests has been carried out.

Furthermore, the test procedure has been proved experimentally utilizing a universal testing machine and a scaled flywheel rotor. The experiment proves the static simulation of the FSBT. Furthermore, the quasistatic FE-simulation results of the flywheel rotor using inertia loads compare well to the experimental data of the static burst test. The assumption of a linear system agrees very well with the measurement results. Also the importance of the radial strength of the used material, especially for thick-walled rotor geometries is shown, which is of major relevance for choosing the correct material and rotor geometry. Hence, the presented test method is a very good controllable and observable possibility to test a high speed FESS rotor in a static way instead of a much more expensive and dangerous dynamic spin up test.

Acknowledgments The presented work is part of the research project “OptimumShapeFlywheel“ and is supported by “Klima- und Energiefonds“ in line with the program “NEUE ENERGIEN 2020“ conducted by the Austrian Research Promotion Agency (FFG).

References

1. Sonnichsen, H.E.: Ensuring spin test safety. Mech Eng **115**(5), 72–77 (1993)
2. Genta, G.: Spin tests on medium energy density flywheels. Composites **13**, 38–46 (1982)

3. Curtiss, D.H., Mongeau, P.P., Puterbaugh, R.L.: Advanced composite flywheel structural design for a pulsed disk alternator. IEEE Trans. Magn. **31**, 26–31 (1995)
4. Ha, S.K., Kim, D.J., Nasir, S.U., Han, S.C.: Design optimization and fabrication of a hybrid composite flywheel rotor. Compos. Struct. **94**, 3290–3299 (2012)
5. Kim, S., Hayat, K., Nasir, S., Ha, S.: Design and fabrication of hybrid composite hubs for a multi-rim flywheel energy storage system. Compos. Struct. **107**, 19–29 (2014)
6. Nagy, G., Rosenwasser, S., Mehle, G.: The evaluation and testing of graphite fiber composite materials for high speed rotors. IEEE Trans. Magn. **31**, 289–293 (1999)
7. Nagy, G., Rosenwasser, S.: The evaluation of advanced composite material performance in high speed pulsed power rotor applications. IEEE Trans. Magn. **37**, 314–317 (2001)
8. Lelos, V., Manifold, S., Granier, J.: Structural properties and testing of a composite banding used in high-speed rotors. IEEE Trans. Magn. **43**, 250–253 (2007)
9. Tzeng, J., Emerson, R., Moy, P.: Composite flywheels for energy storage. Compos. Sci. Technol. **66**, 2520–2527 (2006)
10. Headifen, R.N., Gupta, S., Okey, D.: Experimental testing of thick-walled graphite fiber composite rings. Compos. Sci. Technol. **51**(4), 531–536 (1994)
11. Ahmad, R., Al-Salehi, F.A.R., Al-Hassani, S.T.S., Hinton, M.J.: Strength and failure modes of hoop wound cfrp tubes under compressive high rates of loading. Appl. Compos. Mater. **12**(5), 277–292 (2005)
12. Al-Salehi, F.A.R., Al-Hassani, S.T.S., Haftchenari, H., Hinton, M.J.: Effect of temperature on the tensile strength and failure modes of angle ply cfrp tubes under hoop loading. Appl. Compos. Mater. **5**(5), 319–343 (1998)
13. Al-Salehi, F.A.R., Al-Hassani, S.T.S., Haftchenari, H., Hinton, M.J.: Temperature and rate effects on grp tubes under tensile hoop loading. Appl. Compos. Mater. **8**, 1–24 (2001)
14. Haftchenari, H., Al-Salehi, F.A.R., Al-Hassani, S.T.S., Hinton, M.J.: Effect of temperature on the tensile strength and failure modes of angle ply aramid fibre (krp) tubes under hoop loading. Appl. Compos. Mater. **9**, 99–115 (2002)
15. Schulz, A., Hinterdorfer, T., Sima, H., Wassermann, J., Neumann, M.: FLYWHEEL. WO Patent 2013170284 (A1) (2013)
16. Hinterdorfer, T., Schulz, A., Sima, H., Hartl, S., Wassermann, J.: Topology optimization of a flywheel energy storage rotor using a genetic algorithm. In: Proceedings of the International Symposium on Magnetic Bearings, pp. 11–14. IEEE, Linz, Austria (2014)
17. Hartl, S., Schulz, A., Kaltenbacher, M.: Optimum design of a high energy density composite flywheel rotor. In: Proceedings of the Vienna young Scientists Symposium, pp. 25–26. TU Wien, Wien, Austria (2015)
18. Hartl, S., Schulz, A., Kaltenbacher, M.: Design of a carbon fiber reinforced plastic shaft for a high speed flywheel rotor. In: Proceedings of the International Conference on Composite Materials, pp. 19–24, Cobenhagen, Denmark (2015)
19. Schulz, A., Hartl, S., Sima, H., Hinterdorfer, T., Wassermann, J.: Innovative Schwungradspeicher mit hoher Energieeffizienz und Zuverlässigkeit. Elektrotechnik und Informationstechnik. to be published (2015)
20. Millan, C., Jimenez, M.A., Miravete, A.: Finite element calculation of a press fit joint between a composite materials tube and an aluminium cylinder. Appl. Compos. Mater. **6**(6), 369–380 (2001)
21. Hartl, S., Schulz, A., Kaltenbacher, M.: Direct estimation of the elastic constants of cfrp plates by using lagranges equation. In: Proceedings of the International Conference on Composite Structures, pp. 15–18, Lisbon, Portugal (2015)
22. DIN EN ISO 527-1:2012-06, Kunststoffe - Bestimmung der Zugeigenschaften - Teil 1: Allgemeine Grundsätze (ISO 527-1:2012)
23. DIN EN ISO 527-5:2010-01, Kunststoffe - Bestimmung der Zugeigenschaften - Teil 5: Prüfbedingungen für unidirektional faserverstärkte Kunststoffverbundwerkstoffe (ISO 527-5:2009)
24. DIN EN ISO 14126:2000-12, Faserverstärkte Kunststoffe - Bestimmung der Druckeigenschaften in der Laminatebene (ISO 14126:1999)
25. DIN EN ISO 14129:1998-02, Faserverstärkte Kunststoffe - Zugversuch an 45-Laminaten zur Bestimmung der Schubspannungs/Schubverformungs-Kurve des Schubmoduls in der Lagenebene (ISO 14129:1997)
26. Tsai, S.W.: Theory of Composites Design. Think Composites, Dayton, USA (1992)
27. Sekine, H., Shin, E.: Optimum design of thick-walled multi-layered cfrp pipes to reduce process-induced residual stresses. Appl. Compos. Mater. **6**(5), 289–307 (1999)
28. Smith, P.A., Boniface, L., Glass, N.F.C.: A comparison of transverse cracking phenomena in (0/90)s and (90/0)s cfrp laminates. Appl. Compos. Mater. **5**, 11–23 (1998)

29. Chen, W., Yu, Y., Li, P., Wang, C., Zhou, T., Yang, X.: Effect of new epoxy matrix for t800 carbon fiber/epoxy filament wound composites. Compos. Sci. Technol. **67**, 2261–2270 (2007)
30. Gao, S.L., Mäder, E., Zhandarov, S.F.: Carbon fiber and composites with epoxy resins: topography, fractography and interphases. Carbon **42**(3), 515–529 (2004)
31. Cerny, I., Mayer, R.M.: Fatigue of selected grp composite components and joints with damage evaluation. Compos. Struct. **94**(2), 664–670 (2012)